

First-principles study of defect formation energies in LaOXs_2 ($X = \text{Sb, Bi}$)

Masayuki Ochi and Kazuhiko Kuroki

Department of Physics, Osaka University, Machikaneyama-cho, Toyonaka, Osaka 560-0043, Japan

(Dated: March 23, 2022)

We theoretically investigate defect formation energies in LaOXs_2 ($X = \text{Sb, Bi}$) using first-principles calculation. We find that the oxygen vacancy is relatively stable, where its formation energy is higher in $X = \text{Sb}$ than in $X = \text{Bi}$. An interesting feature of $X = \text{Sb}$ is that the vacancy of the in-plane sulfur atom becomes more stable than in $X = \text{Bi}$, caused by the formation of an Sb_2 dimer and the electron occupation of the impurity energy levels. The formation energies of cation defects and anion-cation antisite defects are positive for the chemical equilibrium condition used in this study. Fluorine likely replaces oxygen, and its defect formation energy is negative for both $X = \text{Sb}$ and Bi , while that for $X = \text{Sb}$ is much higher than $X = \text{Bi}$. Our study clarifies the stability of several point defects and suggests that the in-plane structural instability is enhanced in $X = \text{Sb}$, which seems to affect a structural change caused by some in-plane point defects.

I. INTRODUCTION

High controllability is a key aspect of materials for systematic investigation of their properties. From this viewpoint, LnOXCh_2 ($\text{Ln} = \text{La, Nd, Ce, etc.}; X = \text{Sb, Bi}; Ch = \text{S, Se}$) is an important family of superconductors¹⁻⁸ and thermoelectric materials⁹⁻¹². Their crystal structures consist of the conducting XCh_2 and insulating LnO layers. A rich variety of constituent elements and the existence of several siblings such as $\text{Bi}_4\text{O}_4\text{S}_3$ ¹ and $\text{LaPbBiS}_3\text{O}^{13-16}$ are remarkable features of this family, which enable a systematic control of their electronic structure. In LnOXCh_2 , electron carriers are usually introduced by fluorine substitutional doping for oxygen², or the valence fluctuation of cerium ions for $\text{Ln} = \text{Ce}$ compounds^{17,18}. Since atoms in insulating layers work as a charge reservoir in both ways, the charge carrier can be introduced without a large change in the electronic state of the conducting layers, which is also advantageous for studying their transport properties.

However, it was recently found that it is experimentally difficult to enhance the electrical conductivity in $X = \text{Sb}$ compounds against their robust insulating nature by the ways described above. While several Sb compounds have been successfully synthesized such as Ce(O,F)SbSe_2 ¹⁹, LnOSbSe_2 ($\text{Ln} = \text{La, Ce}$)²⁰, Ce(O,F)Sb(S,Se)_2 ²¹, and $\text{NdO}_{0.8}\text{F}_{0.2}\text{Sb}_{1-x}\text{Bi}_x\text{Se}_2$ ²², it was also found that the electrical conductivity is low in these systems¹⁹⁻²¹. For example, it was reported that the electrical resistivity ρ of CeOSbSe_2 , $\text{CeO}_{0.9}\text{F}_{0.1}\text{SbSe}_2$, and $\text{LaO}_{0.9}\text{F}_{0.1}\text{SbSe}_2$ are $\sim 10^0\text{--}10^1 \Omega \text{ m}$ at room temperature²⁰. While it is smaller than that for LaOSbSe_2 , $\rho \sim 10^3 \Omega \text{ m}$, much lower resistivity is desirable for employing them as superconductors or thermoelectric materials. Since our recent theoretical study predicts that high thermoelectric performance can be realized in $X = \text{As, Sb}$ compounds²³, efficient control of the carrier concentration in Sb compounds is of great importance. In fact, our previous theoretical calculation showed that the stability of the fluorine substitutional doping is lower in $X = \text{Sb}$ than in $X = \text{Bi}$ ²⁴. However, because that study focuses on the relative stability between Sb and Bi compounds and as-

sumes a simple fluorine-rich limit using a relatively small supercell, it is still unclear whether the fluorine substitutional doping is stable even in Sb compounds. In addition, other possible point defects in mother compounds have not been theoretically investigated so far, even for Bi compounds, while they can affect the transport properties. Because of the importance of the efficient carrier control in LnOXCh_2 compounds, a systematic theoretical study on defect formation energies is highly awaited.

In this paper, we present a systematic investigation on point defects in LaOXs_2 ($X = \text{Sb, Bi}$) by first-principles evaluation of their formation energies. We find that anion replacements S_O and O_S are not stable, while V_O and V_S can take place. The formation energy of V_O is higher in $X = \text{Sb}$ than in $X = \text{Bi}$. An interesting feature of $X = \text{Sb}$ is that the vacancy of in-plane sulfur becomes more stable than in $X = \text{Bi}$ by forming an Sb_2 dimer. The formation energies of cation defects, X_S , and S_X are positive for the chemical equilibrium condition used in this study. Fluorine likely replaces oxygen, and its defect formation energy is negative for both $X = \text{Sb}$ and Bi , while that for $X = \text{Sb}$ is much higher than $X = \text{Bi}$. Our study clarifies the stability of several point defects and suggests that the in-plane structural instability is enhanced in $X = \text{Sb}$, which should be essential knowledge to understand and control the materials properties of LaOXs_2 and related compounds by impurity doping.

This paper is organized as follows. In Sec. II, we describe the calculation methods and computational conditions used in this study. Calculated defect formation energies are shown in Sec. III. Section IV is devoted to the conclusion of this study.

II. METHOD

A. Calculation of the defect formation energy

By $N_1 \times N_2 \times N_3$ supercell calculation, the formation energy of a point defect D in charge state q is evaluated

as^{25,26}

$$E_{\text{form}}[D^q; \mathbf{N}](\Delta\epsilon_{\text{F}}) = E[D^q; \mathbf{N}] + E_{\text{corr}}[D^q; \mathbf{N}] - N_1 N_2 N_3 E_{\text{P}} - \sum_i n_i \mu_i + q(\epsilon_{\text{VBM}} + \Delta\epsilon_{\text{F}}), \quad (1)$$

where $\mathbf{N} = (N_1, N_2, N_3)$, $E[D^q; \mathbf{N}]$, $E_{\text{corr}}[D^q; \mathbf{N}]$ and E_{P} represent the supercell size, the total energies of the supercell with the defect, its energy correction described below, and the total energy of the perfect unit cell without any defect, respectively. n_i represents the number of removed (with a sign of $-$) or added (with a sign of $+$) atoms i , the chemical potential of which is denoted as μ_i . ϵ_{VBM} is the energy level of the valence-band maximum (VBM), and $\epsilon_{\text{VBM}} + \Delta\epsilon_{\text{F}}$ represents the Fermi level of the system.

In this study, we considered the energy correction $E_{\text{corr}}[D^q; \mathbf{N}]$ consisting of the following two terms:

$$E_{\text{corr}}[D^q; \mathbf{N}] = E_{\text{pc}}(q; \mathbf{N}) + E_{\text{be}}[D^q]. \quad (2)$$

The first term $E_{\text{pc}}(q; \mathbf{N})$ denotes the point-charge correction^{25,27}, which was evaluated through the Ewald summation for screened Coulomb interaction in a periodic supercell consisting of a single point charge q in a uniform background charge $-q$. The screened Coulomb interaction is represented using the macroscopic static dielectric tensor in the way described in Ref. [28]. As described later in this section, the remaining finite-size error is removed by the extrapolation with respect to the supercell size.

The second term $E_{\text{be}}[D^q]$ in Eq. (2) represents the band-edge correction, which is necessary when one uses a calculation method with a sizable band-gap error, such as the local density approximation and the generalized gradient approximation in density functional theory. We applied the band-edge correction for a shallow defect level as described in Refs. [29,30]. Suppose a point defect D with a charge q_0 does not provide any carrier to the system (e.g., $q_0 = 1$ for F_{O} that represents F^- substitution for O^{2-}), and then we define

$$E_{\text{be}}[D^q] = \begin{cases} (q - q_0)\Delta_{\text{bg}}^{\text{v}} & (q > q_0) \\ (q - q_0)\Delta_{\text{bg}}^{\text{c}} & (q \leq q_0) \end{cases}, \quad (3)$$

where the band-edge correction to the valence band maximum $\Delta_{\text{bg}}^{\text{v}}$ and the conduction band minimum $\Delta_{\text{bg}}^{\text{c}}$ are evaluated by elaborate approximations in first-principles calculation that can provide an accurate band gap, as described in the next section. A relative energy level from the band edge, where the formation energy curves of D^q and D^{q_0} intersect, is kept unchanged by this correction. However, this approximation is not necessarily valid when the impurity levels are not shallow. Thus, we did not consider $E_{\text{be}}[D^q]$ for that case. In the following sections, we mention whether $E_{\text{be}}[D^q]$ was applied for each defect. In any case, the VBM energy in Eq. (1) is defined including this correction:

$$\epsilon_{\text{VBM}} = \epsilon_{\text{VBM}}^0 + \Delta_{\text{bg}}^{\text{v}}, \quad (4)$$

where ϵ_{VBM}^0 is an uncorrected VBM energy. This modification of ϵ_{VBM} changes the origin of $\Delta\epsilon_{\text{F}}$ to the corrected VBM energy. We consider defect formation energies for $\Delta\epsilon_{\text{F}}$ lying between the corrected band edges.

After calculating $E[D^q; \mathbf{N}] + E_{\text{corr}}[D^q; \mathbf{N}]$ in Eq. (1) for a set of supercells with several \mathbf{N} , we performed the least-squares fitting of $E[D^q; \mathbf{N}] + E_{\text{corr}}[D^q; \mathbf{N}]$ by $c_0 + c_1 N^{-1}$, where c_0 and c_1 are coefficients of this fitting, and $N = N_1 N_2 N_3$ (cf. Ref. [25] for the N^{-1} (or equivalently, Ω^{-1} with Ω being the supercell volume) dependence). After determining c_0 and c_1 , we took the $N \rightarrow \infty$ limit, i.e., simply took c_0 , to get the thermodynamic limit. By this procedure, we can get the defect formation energy at the thermodynamic limit,

$$E_{\text{form}}[D^q](\Delta\epsilon_{\text{F}}) = \lim_{N_1, N_2, N_3 \rightarrow \infty} E_{\text{form}}[D^q; \mathbf{N}](\Delta\epsilon_{\text{F}}), \quad (5)$$

which shall be shown in the following sections.

B. Computational conditions

We used the Perdew–Burke–Ernzerhof parametrization of the generalized gradient approximation (PBE-GGA)³² and the projector augmented wave (PAW) method³¹ as implemented in the *Vienna Ab initio Simulation Package*^{33–36}. The core electrons in the PAW potentials were taken as follows: [He] for O and F, [Ne] for S, [Kr]4d¹⁰ for La and Sb, and [Xe]5d¹⁰4f¹⁴ for Bi. The spin-orbit coupling (SOC) was not included unless noted because a huge computational cost is required for supercell calculations including SOC. We performed spin-unpolarized calculation unless noted, also due to high computational cost. For ions with a closed-shell electronic configuration such as F^- , the spin polarization is expected to be unstable. Thus, our approximation likely works well for point defects involving such an ionic state. On the other hand, this is not always the case for some point defects, and we note that our approximation can cause some error in that case. The plane-wave cutoff energy of 500 eV and the Gaussian smearing with the smearing width of 0.15 eV were used. The structural optimization was performed until the Hellmann–Feynman force becomes less than 0.02 eVÅ⁻¹ on each atom. All the calculations were performed at zero temperature and zero pressure.

For calculating O_2 and F_2 molecules, we placed an isolated molecule in a 15 Å × 15 Å × 15 Å cell, and only the atomic coordinates were optimized. Spin-triplet oxygen molecule was calculated using the spin-polarized calculation. For calculating several solid compounds used for evaluating the chemical potential μ_i of each atom i , their crystal structures were optimized by the computational conditions described in the previous paragraph. A sufficiently fine \mathbf{k} -mesh was taken for each material. The lattice parameters and the atomic coordinates were optimized within a constraint of a fixed space group.

For supercell calculations of LaOXs_2 ($X = \text{Sb}, \text{Bi}$), we first optimized both the atomic coordinates and the

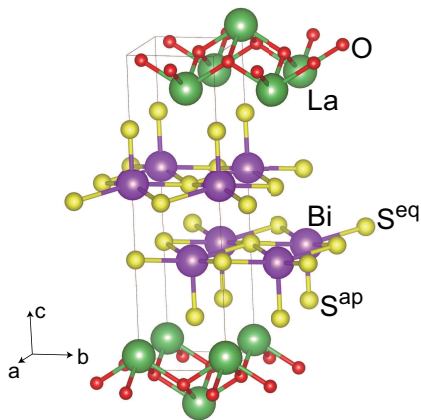


FIG. 1: The crystal structure of LaOBiS₂. Green, red, purple, and yellow spheres represent La, O, Bi, and S atoms, respectively. Lines show the unit cell. All the crystal structures shown in this paper were depicted using the VESTA software⁴⁰.

lattice parameters of the perfect crystal (i.e., without any defect), assuming the space group $P2_1/m$ (monoclinic). This space group was realized in LaOBiS₂^{37–39}. Figure 1 shows the crystal structure of LaOBiS₂. Also for Sb compounds, this space group was experimentally reported for Ce(O,F)SbS₂¹⁹ and Ce(O,F)Sb(S,Se)₂²¹, and was theoretically suggested to be stable for LaOXs₂ ($X = \text{As, Sb, Bi}$)⁴¹ and LaOSbSe₂²⁴. The space group is not necessarily common in $LnOXCh_2$ compounds, because several BiS₂ compounds, such as CeOBiS₂³⁸, and also $LnOSbSe_2$ ($Ln = \text{La, Ce}$)²⁰ were experimentally reported to have the tetragonal $P4/nmm$ space group. Nevertheless, in this study, we can assume $P2_1/m$ in the calculation without loss of generality because this is a subgroup of $P4/nmm$, and found that the crystal structure indeed exhibits the monoclinic distortion as shown in Table I.

After calculating the perfect crystal, we performed the defect calculation by putting an isolated defect in the supercell with different sizes. Here, we considered $3 \times 3 \times 2$, $4 \times 4 \times 2$, and $5 \times 5 \times 2$ supercells, which contain 180, 320, and 500 atoms, respectively. For each supercell, we used $4 \times 4 \times 1$, $3 \times 3 \times 1$, and $3 \times 3 \times 1$ \mathbf{k} -meshes, respectively. Supercell calculation optimized the atomic coordinates using the fixed lattice parameters optimized for the perfect crystal. This treatment is justified because we are interested in the dilute limit of a defect.

For calculating the density of states (DOS), we used $24 \times 24 \times 4$ and $5 \times 5 \times 1$ \mathbf{k} -meshes for the primitive cell and the $4 \times 4 \times 2$ supercell, respectively. We performed these DOS calculations using the fixed charge density obtained in the self-consistent-field (SCF) calculation.

We calculated the macroscopic static dielectric tensor based on the density functional perturbation theory to evaluate the point-charge correction. We considered both the electronic and the ionic contributions of the dielectric tensor. The local field effect for the Hartree and

TABLE I: Optimized lattice parameters of LaOXs₂.

X	a (Å)	b (Å)	c (Å)	β (°)
Sb	4.1018	3.9949	14.112	90.607
Bi	4.0725	4.0505	14.274	91.066

TABLE II: Band-edge correction (eV) for LaOXs₂.

X	$\Delta_{\text{bg}}^{\text{v}}$	$\Delta_{\text{bg}}^{\text{c}}$
Sb	-0.24	-0.07
Bi	-0.35	-0.23

the exchange-correlation potentials was included. The derivative of the cell-periodic part of the Kohn–Sham orbitals were calculated using the finite-difference method using a $12 \times 12 \times 2$ \mathbf{k} -mesh.

For evaluating the band-edge correction, we performed band-structure calculation using the HSE06 hybrid functional⁴² including SOC. Here, we adopt HSE06 because it reproduces the experimental band gap of LaOBiS₂ well: the direct band gap at the X ($= \mathbf{a}^*/2$) point calculated by HSE06+SOC is 0.97 eV, while the experimental optical gap is 1.0 eV⁴³. Band-edge correction was evaluated as an energy difference $\Delta_{\text{bg}} = \epsilon_{\text{HSE06, SOC}} - \epsilon_{\text{PBE, no SOC}}$ for the highest-occupied (for $\Delta_{\text{bg}}^{\text{v}}$) and lowest-unoccupied (for $\Delta_{\text{bg}}^{\text{c}}$) states at the X point, where $\epsilon_{\text{HSE06, SOC}}$ and $\epsilon_{\text{PBE, no SOC}}$ are the orbital energies obtained by HSE06 + SOC and PBE without SOC calculations, respectively. For the HSE06+SOC calculation, we used the crystal structures optimized by PBE calculation without SOC for a fair comparison of the orbital energies. We used a $6 \times 6 \times 1$ \mathbf{k} -mesh for evaluating the band-edge correction. Obtained band-edge corrections are shown in Table II.

While the band-edge correction was applied in the way described in the previous paragraph, the calculation error coming from PBE still remains in our calculation. For example, it is often said that GGA tends to delocalize the electronic state owing to the self-interaction error, which might result in an inaccuracy of the stability for the local structural change and a localized electronic state around it. Such an inaccuracy would be partially removed by using more sophisticated approximations such as the hybrid functionals for structural optimization, which is an important future issue.

III. RESULTS AND DISCUSSION

A. Chemical potentials of atoms

To evaluate the chemical potentials of atoms, μ_i in Eq. (1), we determined possible sets of compounds that can coexist in chemical equilibrium in the following way. Note that the chemical potentials of atoms are not uniquely determined because we can consider different experimental environments such as sulfur-rich and oxygen-poor ones. In this section, we shall show all the

possible equilibriums and then choose a representative one for which we shall present defect formation energies from the next section.

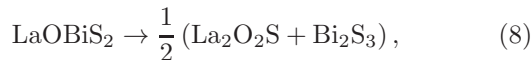
We first calculated the total energies of several solids consisting of La, O, F, Sb, Bi, and S atoms. Table III in Appendix A shows a list of all the compounds considered here. Next, we found out all possible subsets of the compounds, where every compound $\text{La}_v\text{O}_w\text{F}_x\text{X}_y\text{S}_z$ included in a subset satisfies

$$\begin{aligned} E[\text{La}_v\text{O}_w\text{F}_x\text{X}_y\text{S}_z] \\ = v\mu[\text{La}] + w\mu[\text{O}] + x\mu[\text{F}] + y\mu[\text{X}] + z\mu[\text{S}], \end{aligned} \quad (6)$$

while any compound not included in this subset satisfies

$$\begin{aligned} E[\text{La}_v\text{O}_w\text{F}_x\text{X}_y\text{S}_z] \\ > v\mu[\text{La}] + w\mu[\text{O}] + x\mu[\text{F}] + y\mu[\text{X}] + z\mu[\text{S}]. \end{aligned} \quad (7)$$

Here, the chemical potential of an atom is denoted as $\mu[\text{A}]$ for atom A. Each subset consists of five compounds, which enables consistent determination of the atomic chemical potentials using Eq. (6). Note that this procedure was done separately for $X = \text{Sb}$ and Bi. These conditions represent the chemical equilibrium where five compounds included in a subset coexist while other compounds are unstable to exist. For $X = \text{Sb}$, we assumed that LaOSbS_2 is included in every subset. On the other hand, for $X = \text{Bi}$, we found that we cannot include LaOBiS_2 because LaOBiS_2 is slightly unstable with respect to the following reaction,



by 20 meV. This slight instability might be a calculation error or perhaps means that LaOBiS_2 is metastable at zero temperature. It is difficult to discuss such a small energy difference and is outside the scope of this study. Here, instead of including LaOBiS_2 into a subset, we just chose the chemical equilibriums where the instability of LaOBiS_2 is small, by discarding the subsets with $\Delta_{\text{LaOBiS}_2} \equiv E[\text{LaOBiS}_2] - (\mu[\text{La}] + \mu[\text{O}] + \mu[\text{Bi}] + 2\mu[\text{S}]) > 100$ meV. For both $X = \text{Sb}$ and Bi, we also imposed that every subset includes only one fluorine compound. Thanks to this constraint, we can immediately obtain the chemical potentials of La, O, X, and S atoms satisfying the equilibrium condition without fluorine, by simply eliminating the fluorine compound from each subset. This procedure yields the same chemical potentials of La, O, X, and S atoms regardless of the existence of fluorine, which is convenient to compare defect formation energies in chemical equilibrium with and without fluorine.

All possible chemical potentials of atoms, to say, all possible chemical equilibriums, obtained here are listed on Tables IV and V in Appendix A, for LaOSbS_2 and LaOBiS_2 , respectively. Figure 2 summarizes these chemical potentials. For this plot, we defined $\Delta\mu_i \equiv \mu_i - \mu_i^0$ for each atom i , where μ_i^0 is the total energy per atom for La (solid), O_2 molecule, F_2 molecule, Sb (solid), Bi

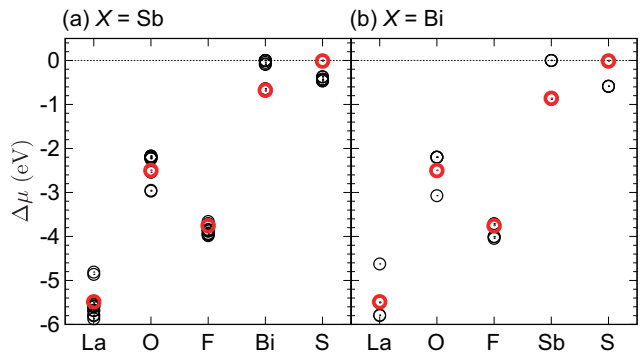


FIG. 2: Chemical potentials of atoms for (a) LaOSbS_2 ($X = \text{Sb}$) and (b) LaOBiS_2 ($X = \text{Bi}$). $\Delta\mu$ is defined in the main text. Red bold circles present the representative values that we used for showing defect formation energies. See the main text for details.

(solid), and $\alpha\text{-S}$ (solid), for La, O, F, Sb, Bi, and S, respectively. As a representative set, we chose the A1 (LaF_3 , La_2S_3 , $\text{La}_2\text{O}_2\text{S}_2$, $\text{La}_2\text{O}_2\text{S}$, and LaOSbS_2) on Table IV for LaOSbS_2 and the B1 (LaF_3 , La_2S_3 , $\text{La}_2\text{O}_2\text{S}_2$, $\text{La}_2\text{O}_2\text{S}$, and Bi_2S_3) on Table V for LaOBiS_2 , the chemical potentials for which are shown by red bold circles in Fig. 2. As shown in Fig. 2, these two chemical equilibriums provide similar values of chemical potentials for LaOSbS_2 and LaOBiS_2 . While we use these chemical potentials in the following subsections, we again note that the chemical potentials of atoms correspond to the experimental environment, which can be controlled by the experimental setup. Thus, calculated defect formation energies presented hereafter can vary by differences in chemical potentials shown in Fig. 2.

Here we briefly mention the consistency between theoretically estimated chemical equilibriums and actual experimental environments for synthesis. It was experimentally reported that $\text{La}_2\text{O}_2\text{S}$ impurity is often found in the synthesis of LaOBiS_2 (e.g., Ref. [43]). LaF_3 is used for introducing fluorine into LaOBiS_2 and is often found as an impurity phase (e.g., Ref. [2]). Also, Bi_2OS_2 , Bi_2S_3 , and Bi impurity phases are found in the synthesis of Bi_2OS_2 , which is a sibling compound of LaOBiS_2 , where La is replaced with Bi in Bi_2OS_2 ⁴³. Given these facts, it seems that our theoretical estimate to some extent represents experimental environments for synthesis.

B. Anion point defects in mother compounds

Formation energies of the anion point defects are shown in Fig. 3. In the figure, point defect species are denoted with the Kröger-Vink notation without showing the electronic charge since it varies against the chemical potential. Lines with the most stable q are shown for each chemical potential. For each line, a value of charge q is shown in the figure. Here, the slope of a line in the figure

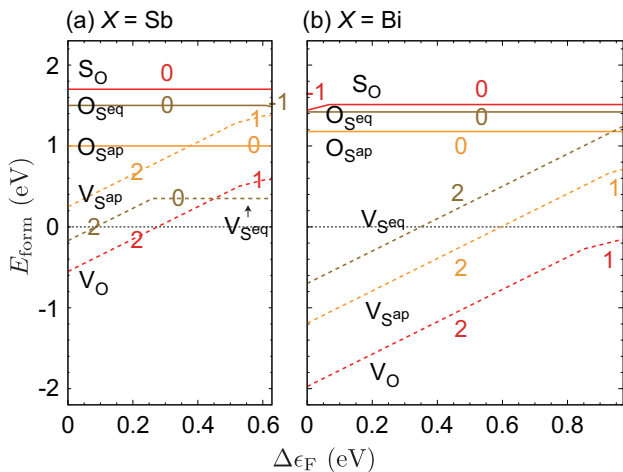


FIG. 3: Defect formation energies E_{form} of anion point defects for (a) LaOSbS₂ ($X = \text{Sb}$) and (b) LaOBiS₂ ($X = \text{Bi}$). The horizontal line (i.e. the Fermi level) is restricted to the energy range between the band edges corrected by HSE06. The values of q , which equals to the slope of each line, are shown beside the line.

equals q (see Eq. (1)). The equatorial and apical sulfur atoms, S^{eq} and S^{ap} , respectively, are defined in Fig. 1. We applied the correction $E_{\text{be}}[D^q]$ except $\text{V}_{\text{S}^{\text{eq}}}$, where the impurity energy level is not shallow, as we shall see later in this section.

In Fig. 3, we can see that S_{O} and O_{S} are relatively unstable compared with V_{O} and V_{S} . For $X = \text{Bi}$, the possible formation of O and S vacancies is consistent with the experimentally observed n-type carriers in the mother compound without fluorine doping. Note that here we adopted the S-rich environment, i.e., a high chemical potential $\mu[\text{S}]$, as shown in Fig. 2, but V_{S} can be lowered by about 0.6 eV for $X = \text{Bi}$ when one adopts the S-poor environment as shown in Fig. 12(c). It is also noteworthy that the oxygen vacancy was experimentally observed in LaOBiSSe⁴⁵. For $X = \text{Sb}$, V_{O} and $\text{V}_{\text{S}^{\text{ap}}}$ become much more unstable than $X = \text{Bi}$, while $\text{V}_{\text{S}^{\text{eq}}}$ becomes much more stable at the conduction bottom with $q = 0$ charge. We adopt the S-rich environment here, but the S-poor environment can lower the V_{S} formation energy by about 0.5 eV as shown in Fig. 12(a), which makes the formation energy of $\text{V}_{\text{S}^{\text{eq}}}$ negative. Also, the formation energy of V_{O} can be almost zero by adopting the O-poor environment.

A negative formation energy for the whole energy range of the Fermi level within the band gap is troublesome from the viewpoint of the materials stability, because a large number of the point defects will be created in that case. We got such a low defect formation energy in some cases, such as V_{O} in Figs. 3(b) and 12(c), V_{S} in Fig. 12(a). One possible reason that makes this situation is the calculation errors, such as the finite-size error and the band-gap inaccuracy, both of which can in general result in an error in the formation energy of an order of

0.1 eV, even if one carefully pays attention to these issues and applies the correction terms. Another possibility is that some sets of the chemical potentials of atoms in Tables IV and V are not appropriate for materials synthesis. Considering the limitation of the accuracy of our calculation method, it is difficult to go into details further. Nevertheless, we again emphasize the consistency between our calculation and experiments where a small amount of electron carriers is observed. If a defect that can introduce the electron carriers into the system has a negative formation energy for some Fermi level (e.g., near the valence band top), the Fermi level is automatically pushed up by the introduced electron carriers. Then, the Fermi level becomes close to the conduction band bottom, while the formation energy should be positive at the conduction band edge for the materials stability. Our calculation results well represent this trend.

Among the point defects investigated in this section, $\text{V}_{\text{S}^{\text{eq}}}$ is interesting in the sense that this defect offers an in-gap impurity state accompanied by a change of the (local) crystal structure. Figure 4 presents the partial DOS and the crystal structure of the XS_2 plane that includes the S^{eq} vacancy. We found that the crystal structures shown in Figs. 4(b)(f) are stable for $q = 2$, while those shown in Figs. 4(d)(h) are stable for $q = 0, 1$. The characteristic change here is the formation of the X_2 dimer in the $q = 0, 1$ structures as shown in Figs. 4(d)(h). Here, the DOS peaks shown with arrows in Figs. 4(a)(c)(e)(g) have a relatively large component of the X_2 dimer. This tendency is clear for Fig. 4(g) while it is not clear for Fig. 4(e), because the Bi-Bi distance surrounded by the broken line in Fig. 4(f) (4.41 Å) is much longer than that in Fig. 4(h) (3.42 Å). A similar situation happens for the Sb compound, where the Sb-Sb distance is 4.08 Å in Fig. 4(b) and 3.04 Å in Fig. 4(d). The bond formation is usually caused by the electron occupation of the bonding orbitals that have low eigenenergies. In fact, the impurity levels with a relatively large X_2 dimer components denoted with arrows are occupied in Figs. 4(c)(g) ($q = 0$), while it is not the case for the $q = 2$ states as shown in Figs. 4(a)(e). The valence electron density for $X = \text{Sb}$ with $q = 0, 2$ shown in Figs. 4(i)(j) also supports the bond formation within such an X_2 dimer for the $q = 0$ case.

It is also noteworthy that the X-S network is strongly disarranged in $X = \text{Sb}$ with $q = 0$ as shown in Fig. 4(d). This notable structural change might be related to the instability of in-plane atoms in BiS₂ compounds observed in experimental studies^{11,44}, which seems more significant in the case of $X = \text{Sb}$.

C. Cation point defects in mother compounds

Formation energies of the cation point defects are shown in Fig. 5. We do not show V_{La} here because we found that its formation energy is too high in the overall range of the chemical potential (e.g., > 4.5 eV for $X =$

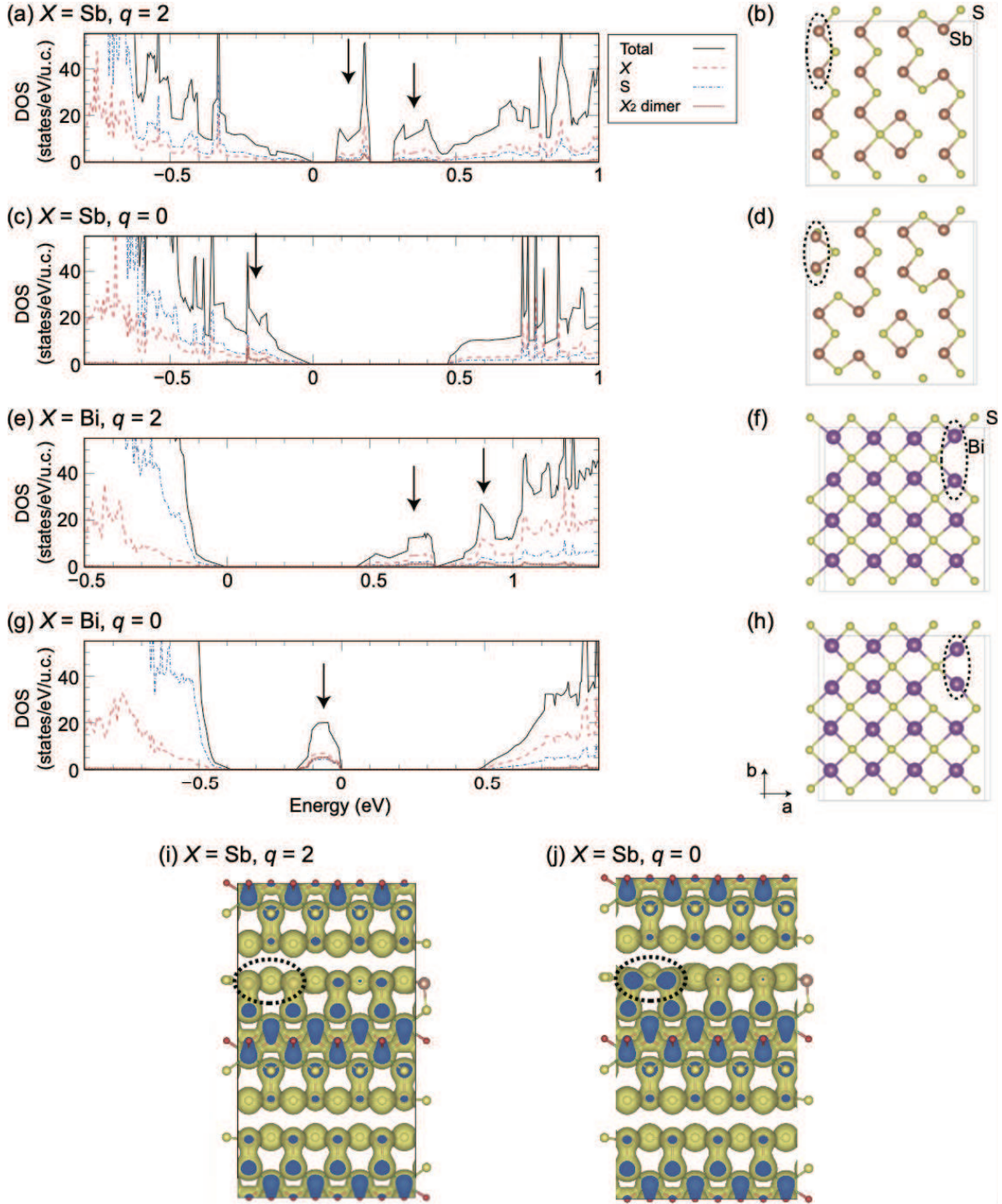


FIG. 4: (a)(c)(e)(g) Partial DOS and (b)(d)(f)(h) the crystal structure of the XS_2 plane that includes the S^{eq} vacancy. (a)(b) $X = \text{Sb}$ with $q = 2$, (c)(d) $X = \text{Sb}$ with $q = 0$, (e)(f) $X = \text{Bi}$ with $q = 2$, and (g)(h) $X = \text{Bi}$ with $q = 0$. The zero of the energy in the DOS plots is the highest occupied energy level for each condition. Some of the impurity levels are shown with arrows in the DOS plots. The partial density of states for the X_2 dimer surrounded by the black broken lines in the crystal structure are shown in the DOS plots. In the crystal structure, brown, purple, and yellow spheres represent Sb, Bi, and S atoms, respectively. The valence electron density is shown for $X = \text{Sb}$ with (i) $q = 2$ and (j) $q = 0$. The black broken lines in panels (i)(j) correspond to those shown in panels (b)(d).

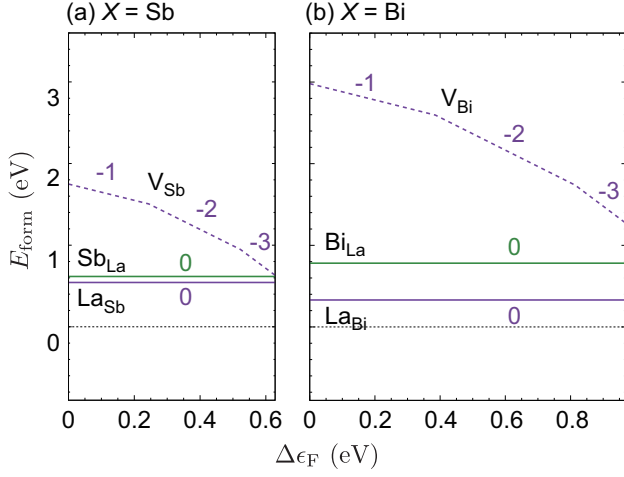


FIG. 5: Defect formation energies E_{form} of cation point defects for (a) LaOSbS_2 ($X = \text{Sb}$) and (b) LaOBiS_2 ($X = \text{Bi}$). The horizontal line (i.e. the Fermi level) is restricted to the energy range between the band edges corrected by HSE06. The values of q , which equals to the slope of each line, are shown beside the line.

Bi). We applied the correction $E_{\text{be}}[D^q]$ except V_X , where the impurity energy level is not shallow, as we shall see later in this section. All the defect formation energies shown in Fig. 5 are positive even at the conduction band bottom.

Here, we briefly discuss how the choice of the atomic chemical potentials can change our conclusion. In Fig. 5, we used an X -poor environment (see Fig. 2 and Tables IV and V). If one uses an X -rich environment, $\mu[\text{Sb}]$ and $\mu[\text{Bi}]$ can be increased by 0.68 and 0.86 eV, respectively, which destabilizes V_X and La_X and stabilizes X_{La} . The energy diagrams for the X -rich conditions are shown in Figs. 13(a)–(d). As for the La chemical potential, we can adopt an La-rich environment but it also leads to a high $\mu[X]$ (X -rich, see A3 and A5 in Table IV and B2 in Table V), which almost does not change the defect formation energies of X_{La} and La_X , as shown in Figs. 13(a)(c). In total, X_{La} can exhibit slightly negative formation energy only for an La-poorer and X -richer environment, as shown in Figs. 13(b)(d). Such a negative formation energy for the Fermi level in the whole energy region of the band gap is troublesome for the materials stability as discussed in the previous section. This situation is possibly due to the calculation error, such as the finite-size error and the band-gap inaccuracy, or means that that chemical environment is not appropriate for materials synthesis. However, even when the system has a small number of X_{La} defects, because of the following three reasons, we do not consider that transport properties are much affected by this defect: X_{La} is a defect in the insulating LaO layer rather than the conducting XS_2 layer, this defect introduces no carriers, and we do not find any in-gap impurity state for this defect.

For the V_X defect that shows a change of q in the in-

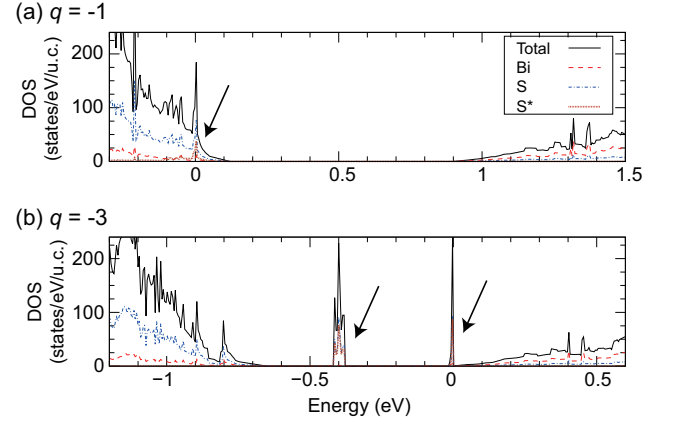


FIG. 6: Partial DOS for the system with V_{Bi} with (a) $q = -1$ and (b) $q = -3$. The zero of the energy in the DOS plots is the Fermi energy for each condition. Some of the impurity levels are shown with arrows. S^* shown in the legend denotes S^{ap} just next to the vacancy site.

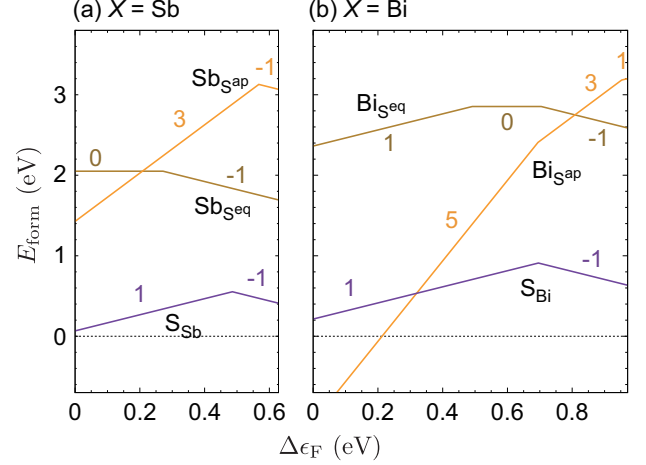


FIG. 7: Defect formation energies E_{form} of X/S or S/X point defects for (a) LaOSbS_2 ($X = \text{Sb}$) and (b) LaOBiS_2 ($X = \text{Bi}$). The horizontal line (i.e. the Fermi level) is restricted to the energy range between the band edges corrected by HSE06. The values of q , which equals to the slope of each line, are shown beside the line.

gap energy region, we present the partial DOS for $X = \text{Bi}$ with $q = -1, -3$ in Fig. 6. There are very sharp DOS peaks that mainly consist of S^{ap} just next to the vacancy site. The energy level of this impurity state can lie within the band gap as shown in Fig. 6(b), which induces the change of q in Fig. 5. To say, $q = -3$ gives electron occupation of such defect states as shown in Fig. 6(b).

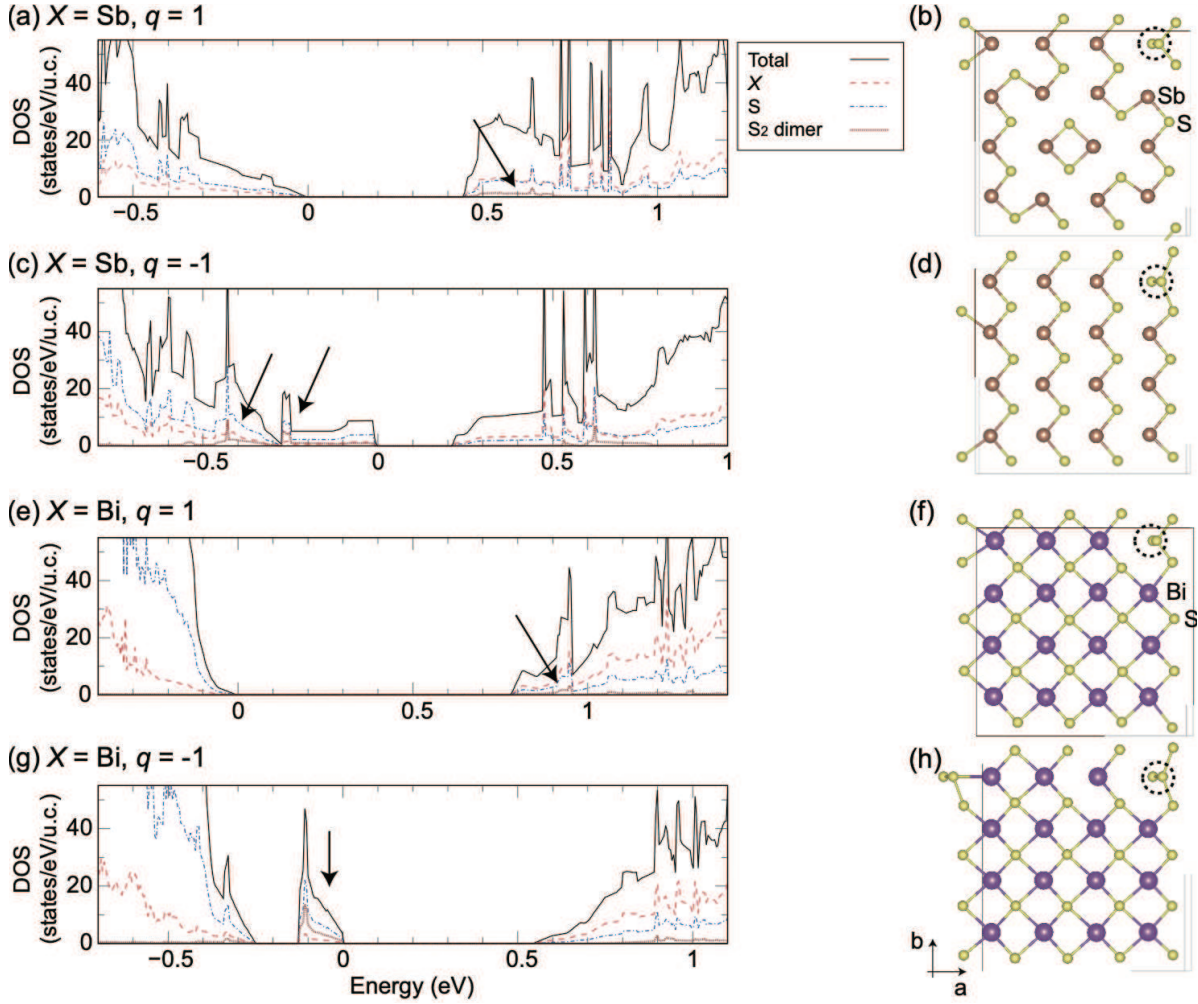


FIG. 8: (a)(c)(e)(g) Partial DOS and (b)(d)(f)(h) the crystal structure of the XS_2 plane that includes the S_X defect. (a)(b) $X = \text{Sb}$ with $q = 1$, (c)(d) $X = \text{Sb}$ with $q = -1$, (e)(f) $X = \text{Bi}$ with $q = 1$, and (g)(h) $X = \text{Bi}$ with $q = -1$. The zero of the energy in the DOS plots is the highest occupied energy level for each condition. Some of the impurity levels are shown with arrows in the DOS plots. The partial density of states for the S_2 dimer surrounded by the black broken lines in the crystal structure are shown in the DOS plots. In the crystal structure, brown, purple, and yellow spheres represent Sb, Bi, and S atoms, respectively.

D. Point defects with X/S or S/X substitution

Formation energies of the point defects of X_S or S_X are shown in Fig. 7. These defects involve an anion-cation exchange, by which we found that many in-gap states take place. Therefore, we did not apply the correction $E_{\text{be}}[D^q]$ for all the point defects investigated in this section.

We can see that the defect formation energies of X_S are all high at the conduction band bottom, where the chemical potential is considered to lie in these n-type materials. Thus, we do not go into details about these defects. On the other hand, the defect formation energy of S_X is relatively low at the conduction band bottom. Figure 8 presents the partial DOS and the crystal struc-

ture of the XS_2 plane that includes the S_X defect. In this case, the impurity level shown in Fig. 8(c)(g) mainly consists of the S_2 dimer surrounded by the black broken lines in Fig. 8(d)(h), respectively. In Fig. 8(d)(h), the S_2 dimer is more separate from the surrounding atoms than that shown in Fig. 8(b)(f), as manifested by the bond angle of in-plane sulfurs. The $q = -1$ charge state allows the occupation of the impurity levels, which seems to stabilize the local structures containing the S_2 dimer more separate from the surrounding atoms. It is also noteworthy that the Sb-S network is again strongly disarranged in Fig. 8(b), as we have seen in Figs. 4(b)(d). This also suggests that the SbS_2 plane is prone to be disordered.

Since here we considered the X -poor and S -rich environment (see Fig. 2), the S_X defect cannot be further

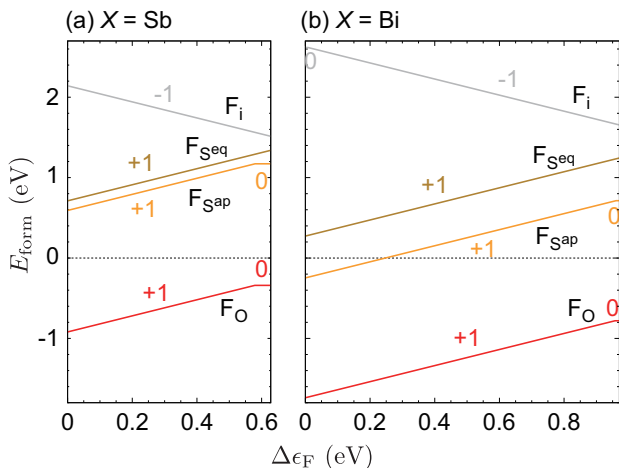


FIG. 9: Defect formation energies E_{form} of fluorine point defects for (a) LaOSbS_2 ($X = \text{Sb}$) and (b) LaOBiS_2 ($X = \text{Bi}$). The horizontal line (i.e. the Fermi level) is restricted to the energy range between the band edges corrected by HSE06. The values of q , which equals to the slope of each line, are shown beside the line.

stabilized by a different choice of the atomic chemical potentials. The X_S defects can be stabilized to some extent, but still has positive formation energy even if one considers the X -rich and S -poor environment, as shown in Fig. 14.

E. Fluorine point defects

Finally, to see the effects of fluorine doping, we calculated fluorine-related point defects as shown in Figs. 9(a)–(b) for LaOSbS_2 and LaOBiS_2 , respectively. We applied the correction $E_{\text{be}}[D^q]$ for all the defects considered here. For interstitial fluorine doping, F_i , Figure 10 shows the most stable position of a fluorine atom we found. Note that we also found that the defect formation energy of F_i for the case when one places a fluorine atom between two XS_2 layers is almost similar. The energy difference between that case and the most stable case is at most 0.15 eV for $X = \text{Sb}$ and 0.02 eV for $X = \text{Bi}$.

It is clearly presented that, for both compounds, the substitutional doping for oxygen, F_O , is the most stable point defect when fluorine is introduced into the crystal. This situation is unchanged by using different sets of chemical potentials of atoms (see Fig. 15). Its charge state is basically F_O^\bullet (i.e., $q = +1$) when the chemical potential lies in the band gap, which is naturally understood by considering that O^{2-} is replaced with F^- . This is consistent with many experimental studies of LaOBiS_2 where fluorine is doped into the crystal to introduce electron carriers². The defect formation energy of F_O is higher in $X = \text{Sb}$, which is consistent with the previous theoretical study²⁴. Even so, it is noteworthy that

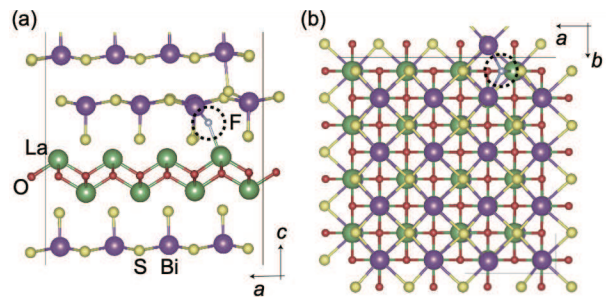


FIG. 10: The position of the interstitial fluorine atom, F_i , is shown in the $4 \times 4 \times 2$ supercell as (a) side view and (b) top view. Green, red, purple, yellow, and white spheres represent La, O, Bi, S, and F atoms, respectively. For both panels, atoms far from the fluorine atom are omitted for visibility.

the defect formation energy of F_O is negative both for LaOSbS_2 and for LaOBiS_2 . In fact, an experimental study found that lattice parameters are changed and the electrical conductivity is to some extent increased by fluorine doping for LaOSbSe_2 ²⁰, which suggests that fluorine was successfully doped into the crystal in experiments. In the following subsection, we discuss why carrier control is still difficult in Sb compounds, even though the fluorine substitutional doping seems to be realized.

We note that the defect formation energy of F_O is close to zero at the conduction band bottom, in particular for $X = \text{Sb}$, which can be positive by using different chemical potentials of atoms, as shown in Fig. 15(b). In addition, the calculation results, of course, should be different for different compounds (i.e., different lanthanoid and chalcogen elements). In this sense, our calculation results suggest that fluorine substitutional doping for oxygen can be energetically unfavorable in some $X = \text{Sb}$ compounds or some experimental setup.

F. Differences between $X = \text{Sb}$ and Bi compounds

Here, we summarize the important differences between $X = \text{Sb}$ and Bi compounds: (i) V_O has a lower formation energy in $X = \text{Bi}$ than in $X = \text{Sb}$. (ii) In-plane structural instability seems to result in the relatively stable $V_{S^{\text{seq}}}$ for $X = \text{Sb}$ (and S_X). The in-plane X - S bonding network is more strongly disarranged for $X = \text{Sb}$. (iii) F_O has a lower formation energy in $X = \text{Bi}$ than in $X = \text{Sb}$.

Both (i) and (iii) suggest that the electron carriers are much more difficult to introduce because of higher formation energies of corresponding point defects in $X = \text{Sb}$ compounds than in $X = \text{Bi}$ compounds. Even when one succeeds in introducing the electron carriers, the strong in-plane structural instability in $X = \text{Sb}$ can be an obstacle for realizing high electrical conductivity, as suggested by (ii). While we have only investigated the point defects in this study, several possible higher-order defects, such as a twin defect, can occur in these compounds. It is an

important future problem to clarify the origins of the relatively low electrical conductivity in $X = \text{Sb}$ compounds from this viewpoint.

G. Some remarks for effective carrier control

Our calculation suggests that the anion vacancy (V_{O} or V_{S}) can be relatively stable in some chemical environment. This observation means that oxygen-rich and sulfur-rich environment can be beneficial to synthesize the crystal with a low concentration of defects. It also means that one can possibly control the electron carrier concentration by changing the chemical potentials of oxygen and sulfur. When one would like to introduce a large amount of electron carriers, the fluorine substitutional doping F_{O} is shown to be effective as is well known in experimental studies of BiS_2 compounds.

IV. CONCLUSION

In this paper, we have systematically investigated the defect formation energy of several point defects in LaOXs_2 ($X = \text{Sb}, \text{Bi}$) using first-principles calculation. We have found that anion replacements S_{O} and O_{S} are not stable while V_{O} and V_{S} can take place, while the formation energy of V_{O} is higher in $X = \text{Sb}$ than in $X = \text{Bi}$. It is characteristic that V_{Seq} becomes much more stable in $X = \text{Sb}$ than in $X = \text{Bi}$, due to the formation of an Sb_2 dimer and the occupation of the impurity energy levels. The formation energies of cation defects, X_{S} , and S_{X} are positive for the atomic chemical potentials used in this study. Fluorine likely replaces oxygen for both $X = \text{Sb}$ and Bi . The defect formation energy of F_{O} is negative for both compounds, while that for $X = \text{Sb}$ is much higher than $X = \text{Bi}$. Our study has clarified the stability of several point defects and suggested that the in-plane structural instability is enhanced in $X = \text{Sb}$. This knowledge should be helpful for understanding and controlling the transport properties of LaOXs_2 and related compounds by impurity doping.

Acknowledgments

We appreciate the fruitful discussion with Yosuke Goto, Yoshikazu Mizuguchi, and Kazutaka Nishiguchi. This study was supported by JST CREST (No. JPMJCR20Q4), Japan. Part of the numerical calculations were performed using the large-scale computer systems provided by the supercomputer center of the Institute for Solid State Physics, the University of Tokyo, and the Information Technology Center, the University of Tokyo.

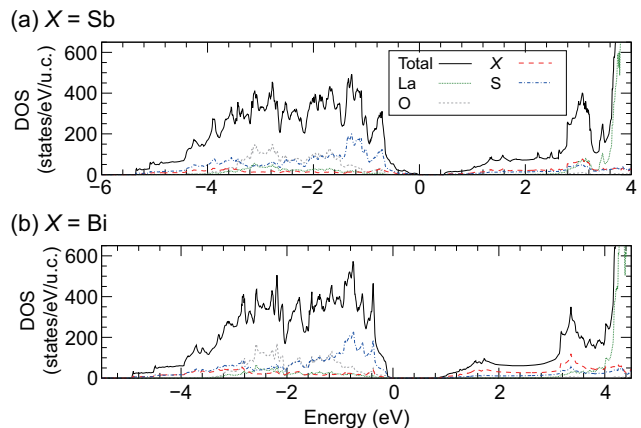


FIG. 11: Partial DOS for perfect crystal of LaOXs_2 : (a) $X = \text{Sb}$ and (b) $X = \text{Bi}$. To compare them with those shown in the main text, DOS is normalized as that for the $4 \times 4 \times 2$ supercell. To say, u.c. = unit cell used for the $4 \times 4 \times 2$ supercell calculation containing 320 atoms.

Appendix A: Density of states for perfect crystal

Figure 11 presents the partial DOS for perfect crystal of LaOXs_2 ($X = \text{Sb}, \text{Bi}$).

Appendix B: Extended data for calculating chemical potentials of atoms

Table III presents a list of solid compounds, which in addition to LaOSbS_2 , were used to determine the chemical potentials of atoms. Since we performed the first-principles calculation at zero temperature, we basically adopted the space group of the low-temperature phase for each compound. For LaOF^{51} , we compared the total energies of β - (rhombohedral, $R\bar{3}m$) and t - (tetragonal, $P4/nmm$) phases, and found that the latter has a bit lower total energy. Thus, we adopted the tetragonal phase here.

Using Table III, we obtained the chemical potentials of atoms as listed on Tables IV and V, for LaOSbS_2 and LaOBiS_2 , respectively. As described in Sec. III A, we defined $\Delta\mu_i \equiv \mu_i - \mu_i^0$ for each atom i , where μ_i^0 is the total energy per atom for La (solid), O_2 molecule, F_2 molecule, Sb (solid), Bi (solid), and α -S (solid), for La, O, F, Sb, Bi, and S, respectively. For LaOBiS_2 , a set of solid compounds with $\Delta_{\text{LaOBiS}_2} \equiv E[\text{LaOBiS}_2] - (\mu[\text{La}] + \mu[\text{O}] + \mu[\text{Bi}] + 2\mu[\text{S}]) > 100$ meV were discarded, because the chemical equilibrium where LaOBiS_2 is much unstable is not appropriate for our purpose. The A1 on Table IV and the B1 on Table V were adopted in our theoretical analysis shown in the main text.

TABLE III: A list of solid compounds used to determine the chemical potentials of atoms.

Compound	Space group	Reference
La	$P6_3/mmc$	[46]
S	$Fddd$	[47]
La ₂ O ₃	$P\bar{3}m1$	[48]
LaF ₃	$P\bar{3}c1$	[49]
La ₂ S ₃	$Pnma$	[50]
LaOF	$P4/nmm$	[51]
La ₂ O ₂ S ₂	$Cmca$	[52]
La ₂ O ₂ S	$P\bar{3}m1$	[53]
La ₂ O ₂ SO ₄	$C2/c$	[54]
Bi	$R\bar{3}m$	[46]
LaBi	$Fm\bar{3}m$	[55]
La ₂ Bi	$I4/mmm$	[55]
La ₄ Bi ₃	$I\bar{4}3d$	[56]
La ₅ Bi ₃	$P63/mcm$	[55]
Bi ₂ O ₃	$P2_1/c$	[57]
Bi ₂ O ₄	$C2/c$	[58]
Bi ₄ O ₇	$P\bar{1}$	[59]
BiF ₃	$Fm\bar{3}m$	[60]
Bi ₂ S ₃	$Pnma$	[61]
BiOF	$P4/nmm$	[62]
Bi ₂ OS ₂	$P4/nmm$	[43]
Bi ₂ O ₂ S	$Pnmm$	[63]
Bi ₂ (SO ₄) ₃	$C2/c$	[64]
Sb	$R\bar{3}m$	[46]
LaSb	$Fm\bar{3}m$	[65]
LaSb ₂	$Cmca$	[66]
La ₂ Sb	$I4/mmm$	[67]
La ₄ Sb ₃	$I\bar{4}3d$	[56]
La ₅ Sb ₃	$P63/mcm$	[68]
Sb ₂ O ₃	$Fd\bar{3}m$	[69]
Sb ₂ O ₄	$Pna2_1$	[70]
Sb ₂ O ₅	$C2/c$	[71]
SbF ₃	$Ama2$	[72]
Sb ₂ S ₃	$Pnma$	[61]
SbOF	$Pnma$	[73]
Sb ₃ O ₄ F	$P2_1/c$	[74]
Sb ₃ O ₂ F ₅	$P2/c$	[74]
Sb ₂ OS ₂	$P\bar{1}$	[75]
Sb ₂ (SO ₄) ₃	$P2_1/c$	[76]
Sb ₂ O(SO ₄) ₂	$P4_12_12$	[77]

Appendix C: Defect formation energy calculated with different sets of chemical potentials

Defect formation energy calculated with different sets of chemical potentials are shown in Figs. 12–15.

- ¹ Y. Mizuguchi, H. Fujihisa, Y. Gotoh, K. Suzuki, H. Usui, K. Kuroki, S. Demura, Y. Takano, H. Izawa, and O. Miura, Phys. Rev. B **86**, 220510(R) (2012).
- ² Y. Mizuguchi, S. Demura, K. Deguchi, Y. Takano, H. Fujihisa, Y. Gotoh, H. Izawa, and O. Miura, J. Phys. Soc. Jpn. **81**, 114725 (2012).
- ³ H. Usui, K. Suzuki, and K. Kuroki, Phys. Rev. B **86**, 220501(R) (2012).
- ⁴ Y. Mizuguchi, J. Phys. Chem. Solids **84**, 34 (2015).
- ⁵ D. Yazici, I. Jeon, B. D. White, and M. B. Maple, Physica C **514**, 218 (2015).
- ⁶ H. Usui and K. Kuroki, Novel Supercond. Mater. **1**, 50 (2015).
- ⁷ Y. Mizuguchi, J. Phys. Soc. Jpn. **88**, 041001 (2019).
- ⁸ K. Suzuki, H. Usui, K. Kuroki, T. Nomoto, K. Hattori,

- and H. Ikeda, J. Phys. Soc. Jpn. **88**, 041008 (2019).
- ⁹ A. Nishida, O. Miura, C.-H. Lee, and Y. Mizuguchi, Appl. Phys. Express **8**, 111801 (2015).
- ¹⁰ Y. Mizuguchi, A. Nishida, A. Omachi, and O. Miura, Cog. Phys. **3**, 1156281 (2016).
- ¹¹ C.-H. Lee, J. Phys. Soc. Jpn. **88**, 041009 (2019).
- ¹² M. Ochi, H. Usui, and K. Kuroki, J. Phys. Soc. Jpn. **88**, 041010 (2019).
- ¹³ Y.-L. Sun, A. Ablimit, H.-F. Zhai, J.-K. Bao, Z.-T. Tang, X.-B. Wang, N.-L. Wang, C.-M. Feng, and G.-H. Cao, Inorg. Chem. **53**, 11125 (2014).
- ¹⁴ Y. Mizuguchi, Y. Hijikata, T. Abe, C. Moriyoshi, Y. Kuroiwa, Y. Goto, A. Miura, S. Lee, S. Torii, T. Kamiyama, C. H. Lee, M. Ochi, and K. Kuroki, Europhys. Lett. **119**, 26002 (2017).

TABLE IV: A list of chemical potentials of atoms determined by chemical equilibrium conditions as described in the main text for $X = \text{Sb}$. Chemical potentials are shown in eV.

Subset	$\Delta\mu[\text{La}]$	$\Delta\mu[\text{O}]$	$\Delta\mu[\text{F}]$	$\Delta\mu[\text{Sb}]$	$\Delta\mu[\text{S}]$	Coexisting compounds											
						LaF ₃	LaOF	La ₂ S ₃	La ₂ O ₂ S ₂	La ₂ O ₂ S	La ₂ O ₂ SO ₄	Sb ₂ S ₃	Sb ₂ OS ₂	Sb ₂ O ₃	Sb	S	LaOSbS ₂
A1	-5.49	-2.50	-3.76	-0.68	-0.01	✓		✓	✓	✓							✓
A2	-5.50	-2.49	-3.75	-0.69	0.00	✓		✓	✓							✓	✓
A3	-4.81	-2.95	-3.98	0.00	-0.46	✓		✓		✓						✓	✓
A4	-5.50	-2.54	-3.75	-0.64	0.00	✓		✓				✓				✓	✓
A5	-4.86	-2.97	-3.96	0.00	-0.43	✓		✓				✓				✓	✓
A6	-5.53	-2.23	-3.95	0.00	-0.46		✓		✓					✓	✓	✓	✓
A7	-5.60	-2.23	-3.87	0.00	-0.43		✓					✓	✓		✓	✓	✓
A8	-5.60	-2.23	-3.88	0.00	-0.43		✓						✓	✓	✓	✓	✓
A9	-5.79	-2.20	-3.72	-0.68	-0.01		✓		✓	✓		✓				✓	✓
A10	-5.80	-2.20	-3.71	-0.69	0.00		✓		✓			✓				✓	✓
A11	-5.57	-2.20	-3.93	-0.04	-0.44		✓		✓					✓		✓	✓
A12	-5.87	-2.17	-3.66	-0.64	0.00		✓					✓				✓	✓
A13	-5.69	-2.17	-3.84	-0.09	-0.37		✓					✓	✓			✓	✓
A14	-5.68	-2.18	-3.85	-0.08	-0.38		✓					✓	✓	✓		✓	✓

TABLE V: A list of chemical potentials of atoms determined by chemical equilibrium conditions as described in the main text for $X = \text{Bi}$. For each set of compounds, $\Delta_{\text{LaOBiS}_2} \equiv E[\text{LaOBiS}_2] - (\mu[\text{La}] + \mu[\text{O}] + \mu[\text{Bi}] + 2\mu[\text{S}])$ is also shown. All values are shown in eV.

Subset	$\Delta\mu[\text{La}]$	$\Delta\mu[\text{O}]$	$\Delta\mu[\text{F}]$	$\Delta\mu[\text{Bi}]$	$\Delta\mu[\text{S}]$	Δ_{LaOBiS_2}	Coexisting compounds										
							LaF ₃	LaOF	La ₂ S ₃	La ₂ O ₂ S ₂	La ₂ O ₂ S	La ₂ O ₂ SO ₄	Bi ₂ S ₃	Bi ₂ OS ₂	Bi	S	
B1	-5.49	-2.50	-3.76	-0.86	-0.01	0.02	✓		✓	✓	✓				✓		
B2	-4.63	-3.07	-4.04	0.00	-0.59	0.02	✓		✓	✓	✓				✓		✓
B3	-5.50	-2.49	-3.75	-0.88	0.00	0.03	✓		✓	✓					✓		✓
B4	-5.50	-2.20	-4.01	0.00	-0.59	0.02		✓			✓	✓		✓	✓		✓
B5	-5.79	-2.20	-3.72	-0.86	-0.01	0.02		✓		✓	✓	✓		✓	✓		✓
B6	-5.50	-2.20	-4.00	0.00	-0.59	0.02		✓				✓	✓		✓	✓	✓
B7	-5.80	-2.20	-3.71	-0.88	0.00	0.03		✓		✓		✓	✓		✓		✓

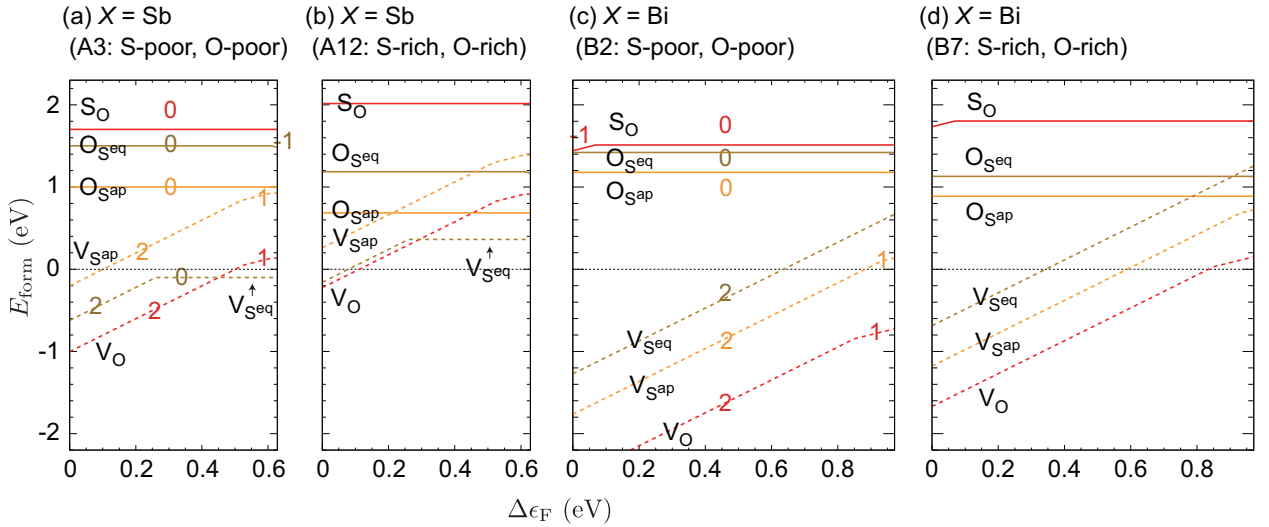


FIG. 12: Defect formation energies E_{form} of anion point defects for (a)(b) LaOSbS_2 ($X = \text{Sb}$) and (c)(d) LaOBiS_2 ($X = \text{Bi}$). The horizontal line is restricted to the energy range between the band edges corrected by HSE06. The values of q , which equals to the slope of each line, are shown beside the line. Sets of the chemical potentials of atoms, A3, A12 shown in Table IV and B2, B7 shown in Table V are used for panels (a)–(d), respectively.

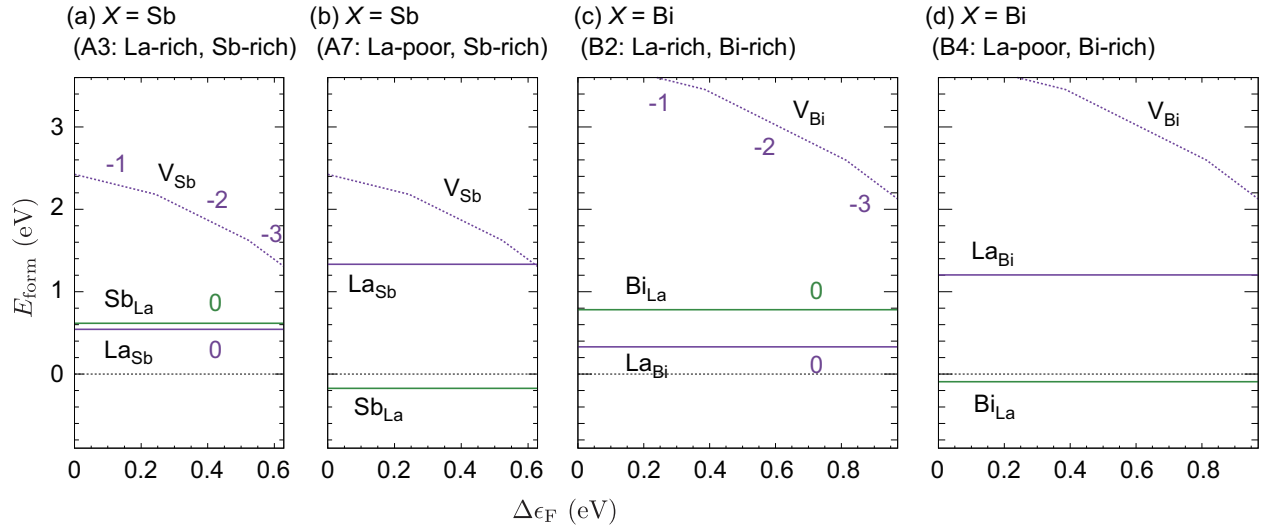


FIG. 13: Defect formation energies E_{form} of cation point defects for (a)(b) LaOSbS_2 ($X = \text{Sb}$) and (c)(d) LaOBiS_2 ($X = \text{Bi}$). The horizontal line is restricted to the energy range between the band edges corrected by HSE06. The values of q , which equals to the slope of each line, are shown beside the line. Sets of the chemical potentials of atoms, A3, A7 shown in Table IV and B2, B4 shown in Table V are used for panels (a)–(d), respectively.

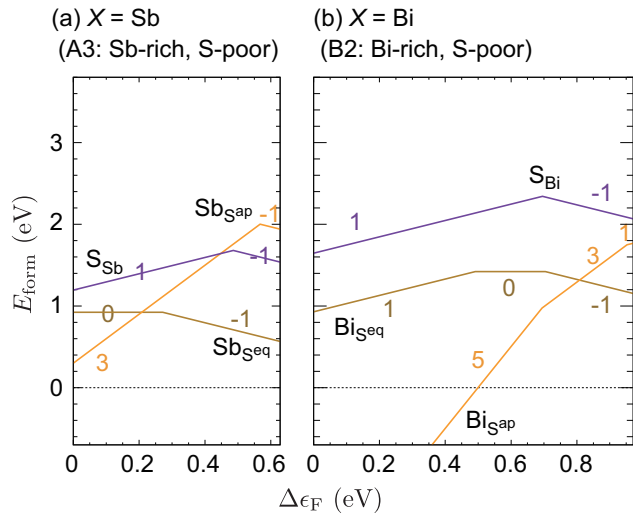


FIG. 14: Defect formation energies E_{form} of X/S or S/X point defects for (a) LaOSbS_2 ($X = \text{Sb}$) and (b) LaOBiS_2 ($X = \text{Bi}$). The horizontal line is restricted to the energy range between the band edges corrected by HSE06. The values of q , which equals to the slope of each line, are shown beside the line. Sets of the chemical potentials of atoms, A3 shown in Table IV and B2 shown in Table V are used for panels (a)–(d), respectively.

15 Y. Yu, C. Wang, Q. Li, C. Cheng, S. Wang, and C. Zhang, *Ceram. Int.* **45**, 817 (2019).
 16 K. Kurematsu, M. Ochi, H. Usui, and K. Kuroki, *J. Phys. Soc. Jpn.* **89**, 024702 (2020).
 17 T. Sugimoto, B. Joseph, E. Paris, A. Iadecola, T. Mizokawa, S. Demura, Y. Mizuguchi, Y. Takano, and N. L. Saini, *Phys. Rev. B* **89**, 201117(R) (2014).
 18 A. Miura, M. Nagao, T. Takei, S. Watauchi, Y. Mizuguchi, Y. Takano, I. Tanaka, and N. Kumada, *Cryst. Growth Des.* **15**, 39 (2015).
 19 M. Nagao, M. Tanaka, R. Matsumoto, H. Tanaka, S. Watauchi, Y. Takano, and I. Tanaka, *Cryst. Growth Des.* **16**, 3037 (2016).
 20 Y. Goto, A. Miura, R. Sakagami, Y. Kamihara, C. Moriyoshi, Y. Kuroiwa, and Y. Mizuguchi, *J. Phys. Soc. Jpn.* **87**, 074703 (2018).
 21 M. Nagao, M. Tanaka, A. Miura, M. Kitamura, K. Horiba, S. Watauchi, Y. Takano, H. Kumigashira, and I. Tanaka, *Solid State Commun.* **289**, 38 (2019).
 22 Y. Goto, A. Miura, C. Moriyoshi, Y. Kuroiwa, and Y. Mizuguchi, *J. Phys. Soc. Jpn.* **88**, 024705 (2019).
 23 M. Ochi, H. Usui, and K. Kuroki, *Phys. Rev. Appl.* **8**, 064020 (2017).
 24 N. Hirayama, M. Ochi and K. Kuroki, *Phys. Rev. B* **100**, 125201 (2019).
 25 H.-P. Komsa, T. T. Rantala, and A. Pasquarello, *Phys. Rev. B* **86**, 045112 (2012).
 26 S. B. Zhang and J. E. Northrup, *Phys. Rev. Lett.* **67**, 2339 (1991).
 27 G. Makov and M. C. Payne, *Phys. Rev. B* **51**, 4014 (1995).
 28 R. Rurali and X. Cartoixa, *Nano Lett.* **9**, 975 (2009).
 29 C. Persson, Y.-J. Zhao, S. Lany, and A. Zunger, *Phys. Rev. B* **72**, 035211 (2005).
 30 S. Lany and A. Zunger, *Phys. Rev. B* **78**, 235104 (2008).

31 G. Kresse and D. Joubert, *Phys. Rev. B* **59**, 1758 (1999).
 32 J. P. Perdew, K. Burke, and M. Ernzerhof, *Phys. Rev. Lett.* **77**, 3865 (1996).
 33 G. Kresse and J. Hafner, *Phys. Rev. B* **47**, 558(R) (1993).
 34 G. Kresse and J. Hafner, *Phys. Rev. B* **49**, 14251 (1994).
 35 G. Kresse and J. Furthmüller, *Comput. Mater. Sci.* **6**, 15 (1996).
 36 G. Kresse and J. Furthmüller, *Phys. Rev. B* **54**, 11169 (1996).
 37 T. Tomita, M. Ebata, H. Soeda, H. Takahashi, H. Fujihisa, Y. Gotoh, Y. Mizuguchi, H. Izawa, O. Miura, S. Demura, K. Deguchi, and Y. Takano, *J. Phys. Soc. Jpn.* **83**, 063704 (2014).
 38 R. Sagayama, H. Sagayama, R. Kumai, Y. Murakami, T. Asano, J. Kajitani, R. Higashinaka, T. D. Matsuda, and Y. Aoki, *J. Phys. Soc. Jpn.* **84**, 123703 (2015).
 39 M. Ochi, R. Akashi, and K. Kuroki, *J. Phys. Soc. Jpn.* **85**, 094705 (2016).
 40 K. Momma and F. Izumi, *J. Appl. Crystallogr.* **44**, 1272 (2011).
 41 Q. Liu, X. Zhang, and A. Zunger, *Phys. Rev. B* **93**, 174119 (2016).
 42 A. V. Krukau, O. A. Vydrov, A. F. Izmaylov, and G. E. Scuseria, *J. Chem. Phys.* **125**, 224106 (2006).
 43 A. Miura, Y. Mizuguchi, T. Takei, N. Kumada, E. Magome, C. Moriyoshi, Y. Kuroiwa, and K. Tadanaga, *Solid State Commun.* **227** 19 (2016).
 44 A. Athauda and D. Louca, *J. Phys. Soc. Jpn.* **88**, 041004 (2019).
 45 J. Shu, H. Yang, Y. Liu, S. Liu, Z. Wen, Y. Cui, Y. Chen, and Y. Zhao, *J. Supercond. Nov. Magn.* **34**, 981 (2021).
 46 R. W. G. Wyckoff, *Crystal Structures* vol. 1 2nd ed. (Interscience Publishers, New York, USA, 1963).
 47 B. E. Warren and J. T. Burwell, *J. Chem. Phys.* **3**, 6 (1935).
 48 W. C. Koehler and E. O. Wollan, *Acta Cryst.* **6**, 741 (1953).
 49 A. Zalkin and D. H. Templeton, *Acta Cryst.* **B41**, 91 (1985).
 50 P. Basançon, C. Adolphe, J. Flahaut, and P. Laruelle, *Mater. Res. Bull.* **4**, 227 (1969).
 51 J. Dabachi, M. Body, J. Dittmer, F. Fayon, and C. Legein, *Dalton Trans.* **44**, 20675 (2015).
 52 J. Ostorero and M. Leblanc, *Acta Cryst.* **C46**, 1376 (1990).
 53 W. H. Zachariasen, *Acta Crystallogr.* **2**, 60 (1949a).
 54 S. Zhukov, A. Yatsenko, V. Chernyshev, V. Trunov, E. Tserkovnaya, O. Antson, J. Hölsä, P. Baulés, and H. Schenk, *Mater. Res. Bull.* **32**, 43 (1997).
 55 K. Yoshihara, J. B. Taylor, L. D. Calvert, and J. G. Despault, *J. Less Common Metals* **41**, 329 (1975).
 56 R. J. Gambino, *J. Less Common Metals* **12**, 344 (1967).
 57 G. Malmros, *Acta Chem. Scand.* **24**, 384 (1970).
 58 N. Kumada, N. Kinomura, P. W. Woodward, and A. W. Sleight, *J. Solid State Chem.* **116**, 281 (1995).
 59 R. E. Dinnebier, R. M. Ibberson, H. Ehrenberg, and M. Jansen, *J. Solid State Chem.* **163**, 332 (2002).
 60 F. Hund and R. Fricke, *Z. Anorg. Allg. Chem.* **258**, 198 (1949).
 61 A. Kyono and M. Kimata, *Am. Mineral.* **89**, 932 (2004).
 62 B. Aurivillius, *Acta Chem. Scand.* **18**, 1823 (1964).
 63 E. Koyama, I. Nakai, and K. Nagashima, *Acta Cryst.* **B40**, 105 (1984).
 64 C. V. Subban, G. Rouse, M. Courty, P. Barboux, and J.-M. Tarascon, *Solid State Sci.* **38**, 25 (2014).

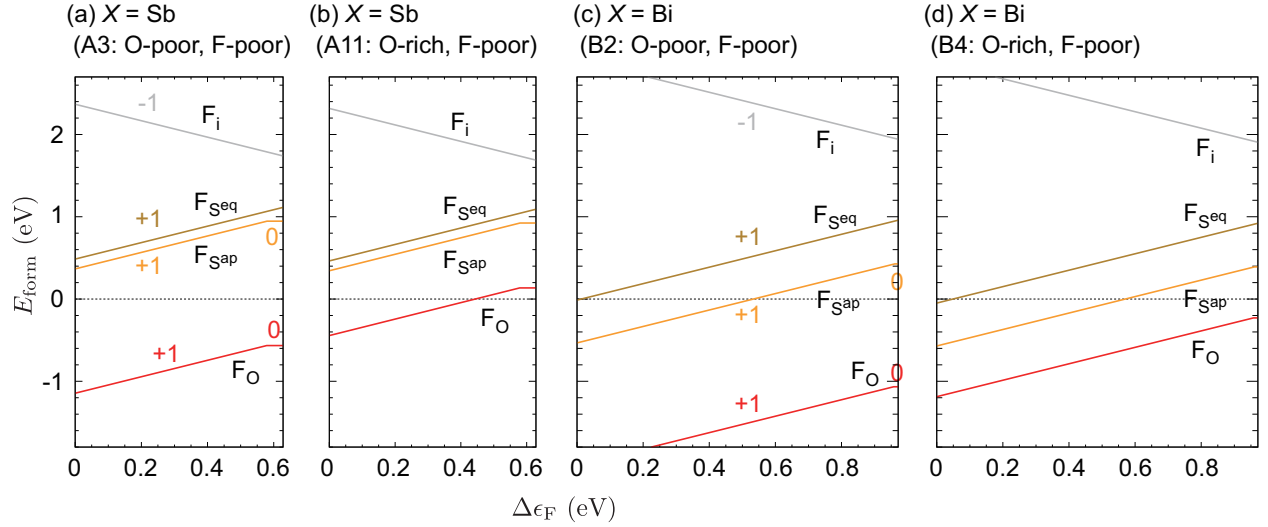


FIG. 15: Defect formation energies E_{form} of fluorine point defects for (a)(b) LaOSbS_2 ($X = \text{Sb}$) and (c)(d) LaOBiS_2 ($X = \text{Bi}$). The horizontal line is restricted to the energy range between the band edges corrected by HSE06. The values of q , which equals to the slope of each line, are shown beside the line. Sets of the chemical potentials of atoms, A3, A11 shown in Table IV and B2, B4 shown in Table V are used for panels (a)–(d), respectively.

- ⁶⁵ A. Iandelli and R. Botti, *Atti Accad. Nazl. Lincei Rend. Classe Sci. Fis. Mat. Nat.* **25**, 498 (1937).
⁶⁶ R. Wang and H. Steinfink, *Inorg. Chem.* **6**, 1685 (1967).
⁶⁷ W. N. Stassen, M. Sato, and L. D. Calvert, *Acta Cryst.* **B26**, 1534 (1970).
⁶⁸ W. Rieger and E. Parthé, *Acta Cryst.* **B24**, 456 (1968).
⁶⁹ R. M. Bozorth, *J. Am. Chem. Soc.* **45**, 1621 (1923).
⁷⁰ P. S. Gopalakrishnan and H. Manohar, *Cryst. Struct. Commun.* **4**, 203 (1975).
⁷¹ M. Jansen, *Acta Cryst.* **B35**, 539 (1979).

- ⁷² A. J. Edwards, *J. Chem. Soc. A*, 2751 (1970).
⁷³ A. Åström and S. Andersson, *Acta Chem. Scand.* **25**, 1519 (1971).
⁷⁴ S. I. Ali and M. Johnsson, *Dalton Trans.* **45**, 12167 (2016).
⁷⁵ J. Hybler and S. Āurovič, *Acta Cryst.* **B69**, 570 (2013).
⁷⁶ R. Mercier, J. Douglade, and J. Bernard, *Acta Cryst.* **B32**, 2787 (1976).
⁷⁷ R. Mercier, J. Douglade, and F. Theobald, *Acta Cryst.* **B31**, 2081 (1975).